

The variable shadow of M87*

Time-resolved interferometric imaging

Philipp Arras, Philipp Frank, Philipp Haim, Jakob Knollmüller,
Reimar Leike, Martin Reinecke, Torsten Enßlin

November 15, 2021

Observing the dynamics of compact astrophysical objects provides insights into their inner workings and allows to probe physics under extreme conditions. The immediate vicinity of an active supermassive black hole with its event horizon, photon ring, accretion disk, and relativistic jets is a perfect place to study general relativity, magneto-hydrodynamics, and high energy plasma physics. The recent observations of the black hole shadow of M87* with *Very Long Baseline Interferometry* (VLBI) by the *Event Horizon Telescope* (EHT) open the possibility to investigate dynamical processes there on timescales of days. In this regime, radio astronomical imaging algorithms are brought to their limits. Compared to regular radio interferometers, VLBI networks have fewer antennas. The resulting sparser sampling of the Fourier sky can only be partly compensated by co-adding observations from different days, as the source changes. Here, we present an imaging algorithm¹ that copes with the data scarcity and the source’s temporal evolution, while simultaneously providing uncertainty quantification on all results. Our algorithm views the imaging task as a Bayesian inference problem of a time-varying flux density, exploits the correlation structure between time frames, and reconstructs a whole, $2 + 1 + 1$ dimensional time-variable and spectral-resolved image at once. We apply the method to the EHT observation of M87* [1] and validate our approach on synthetic data. The obtained first time-resolved reconstruction of M87* indicates varying structures on and outside the emission ring on a time scale of days.

To address the imaging challenge of time-resolved VLBI and in particular of the EHT data, we employ Bayesian inference. In particular, we adopt the formalism of *information field theory* (IFT) [2] for the inference of field-like quantities such as the sky brightness. IFT combines the measurement data and any included prior information into a consistent sky brightness reconstruction and propagates the remaining uncertainties into all final science results. Assuming limited spatial, frequency, and temporal variation we can work with such highly incomplete data as the 2017 EHT observation of M87*.

A related method based on a Gaussian Markov model was proposed by [3]. This method also imposes correlations in space and time, but in our approach the correlation is not fixed and can flexibly adapt to the demands of the data. We also enforce strict positivity of the flux and instead of maximizing posterior probability we perform a variational approximation, taking correlations between all model parameters into account.

¹https://gitlab.mpcdf.mpg.de/ift/vlbi_resolve

The data of interferometric observations essentially consists of the source brightness distribution, Fourier transformed within the image plane and probed only sparsely at a limited number of locations. The measured Fourier modes, called visibilities, are determined by the orientation and distance of antenna pairs, while the Earth rotation helps to partly fill in the gaps by moving these baselines relative to the source. For a time-variable source, this coverage in Fourier coordinates is extremely sparse, as now measurements at different times are looking at a changed source and need to be represented by separate image frames. In the case of the EHT observation of M87*, data was taken only during four 8-hour cycles spread throughout seven days. All the missing image information needs to be restored by the imaging algorithm exploiting implicit and explicit assumptions about the source structure.

Fortunately, most sources, including M87*, do not change completely from one instance to another and subsequent image frames are strongly correlated. Such correlations can be used to inform image degrees of freedom (DOFs) that are not directly constrained by the data. In radio interferometric imaging, correlations are usually enforced by convolving the image with a kernel, either during imaging or afterwards. The specific structure of such a kernel can have substantial impact on the image reconstruction.

To reduce the risk of biasing our result by choosing an inappropriate kernel, our algorithm infers the correlation kernel of the logarithmic flux density in a non-parametric fashion simultaneously with the image. This renders the reconstruction exceptionally hard, as it introduces redundancies between DOFs of the convolution kernel and those of the pre-convolution image. The induction of redundant DOFs is challenging, as the inference has to account for their strongly intertwined uncertainties. Those correlations are essential, but accounting for them is expensive due to the quadratic scaling of their number with the model DOFs.

An inference algorithm capable of tracking uncertainty correlations between all involved DOFs that has only linearly growing memory requirements is *Metric Gaussian Variational Inference* [4, MGVI]. MGVI represents uncertainty correlation matrices implicitly without the need for an explicit storage of their entries. It provides uncertainty quantification of the final reconstruction in terms of samples drawn from the Bayesian posterior distribution, with a moderate level of approximation. MGVI is the central inference engine of the Python package *Numerical Information Field Theory* [5, NIFTy]², which we use to implement our imaging algorithm as it permits the flexible implementation of complex hierarchical Bayesian models. NIFTy turns a forward data model into the corresponding backward inference of the model parameters with the use of automatic differentiation and MGVI.

For time-resolved VLBI imaging, we therefore need to specify the corresponding data model and implement it in NIFTy. This model encodes all physical knowledge about the measurement process and the brightness distribution of the sky, which we decide to take into account to guide and inform the image reconstruction.

For the sky brightness, we require strictly positive structures with characteristic correlations in space, time, and frequency. These brightness fluctuations can vary exponentially over linear distances and time intervals. These properties are represented by a log-normal distribution together with a Gaussian process prior on the logarithmic flux. The correlation structure of this process is assumed here to be homogeneous and isotropic in space, autonomous in time, and independent between space and time.

Consequently the spatial and temporal correlations are represented by a rotationally symmetric convolution kernel, or equivalently by a one-dimensional, isotropic power spectrum in Fourier space. As power spectra are typically close to power laws, we model them as relatively stiff integrated Wiener processes on a double logarithmic scale. Their DOFs, which finally determine the

²<https://gitlab.mpcdf.mpg.de/ift/nifty>

spatio-temporal correlation kernel, are inferred by the MGVI algorithm alongside the sky brightness distribution. While the adopted model can only describe homogeneous and isotropic correlations, this symmetry is broken for the sky image itself by the data, which in general enforces heterogeneous and anisotropic structures. For frequency resolved imaging, we also need to specify the frequency correlation structure. The EHT collaboration has published data averaged down to two frequency bands at about 227 and 229 GHz. Accordingly, we reconstruct two separate, but cross-correlated, images for the these bands, with a priori assumed log-normal deviation on the 1% level. A detailed description of the sky model is outlined in the methods section.

Reconstructing an image with MGVI further requires an accurate model of the instrument that provided the data. Just as the prior model is informed by our physical knowledge of the source, the instrument model is informed by our knowledge of the instrument. We model two sources of measurement noise, which cause the observed visibilities to differ from the perfect sky visibilities: additive Gaussian thermal noise and multiplicative, systematic measurement errors.

The magnitude of the thermal noise is provided by the EHT collaboration in the data set. Systematic measurement errors are mainly caused by antenna-based effects, e.g. differences in the measurement equipment, ionospheric phase shift, and absorption of the incoming electromagnetic waves. Those are described by a complex number per telescope, consisting of the antenna gain factors and antenna phases. In principle it is possible to learn the gain factors as part of the imaging process [6], or by using calibration targets and self-calibration in between imaging iterations.

For VLBI, however, systematic effects are so severe that a different strategy is advantageous. Combinations of visibilities that are invariant under antenna-based systematic effects are formed and used as the data. These are given by the so-called closure phases and closure amplitudes [7], which we briefly discuss in the methods section.

So far, we presented a generic method for time and frequency resolved VLBI imaging. As the immediate vicinity around the super-massive black hole M87* is expected to be dynamic and to exhibit variable emission on a time scale of days, it constitutes an excellent first test case for our method. This variability was confirmed by the EHT, whose exceptional angular resolution allowed for the first time to directly image the shadow of this super-massive black hole. We compare our results to theirs [8–13]. In this letter, we present the first time-resolved reconstruction of the shadow of M87* over the entire observational cycle of seven days. All information on the unit of flux is lost when closure quantities are formed. We therefore fix this unit such that the inside of the ring of Figure 1 is constant in time and agrees with the results of the EHT collaboration for the first frame of our reconstruction. Our two frequency images do not differ significantly. Therefore, our discussion focuses on their mean.

The posterior mean image for the first observing day is shown in Figure 2 together with its pixel-wise posterior uncertainty. In full agreement with the EHT result, our image shows a bright emission ring. We also find the ring to be brighter on its southern part, most likely due to relativistic beaming effects. A saturated version of our and the EHT-imaging shown in Figure 2 highlights morphological differences. In our images the ring is slightly more structured and shows smaller regions of enhanced emission. Outside the ring, only two of the multiple extended structures remain. These have enlarged fluxes, significantly above the posterior uncertainty and therefore are requested by the data.

Figure 1 shows time frames for each day of the observation and their differences. These exhibit mild temporal evolution with flux changes of up to 6% per day, in particular within the western and southern part of the ring, validating the observations made by [11]. Figure 3 shows the detailed temporal evolution of a selected number of locations and areas. For most, there is a good agreement to the EHT results, but for some, clearly visible and significant differences exist. The time evolution of fluxes for the ensemble of posterior samples, also shown in Figure 3, indicates that the flux is

almost time-invariant in most locations. For location 7, which corresponds to the brighter flux region outside the ring, all 40 samples show a consistently declining flux. Here we might witness temporal evolution.

Following the analysis of [11], we compute empirical parameters describing the asymmetric ring, the diameter d , width w , orientation angle η , azimuthal brightness asymmetry A , and floor-to-ring contrast ratio f_C . Table 1 summarises our findings. For the uncertainty quantification, Table 1 displays the results of two different approaches. First, we follow the procedure of [11] with our posterior mean. Second, we perform the same analysis on every sample individually, and then calculate means and variances. The parameter values agree within the uncertainties between the different methods. Their uncertainties differ, but typically by factors of less than two. We can therefore confirm the findings of [11] that diameter d , width w , azimuthal brightness asymmetry A and floor-to-ring contrast ratio f_C are all consistent with being stationary during the seven days, whereas the orientation angle η exhibits a significant time evolution. In this sense, we can report temporal variability of the ring itself. These might be caused by flickering of emission spots [14].

The method section contains further results. Figure 4 provides validation results for our method using three synthetic data sets. Figure 5 shows spatial correlation spectra for our scientific and validation images. Figure 6 displays EHT-imaging, our posterior mean, and two samples for all observation periods.

In conclusion, we present and validate an imaging method that is capable of simultaneously reconstructing emission over spatial, temporal and spectral dimensions. With our method, we largely confirm the findings of the EHT collaboration, the overall morphology of the emission ring around M87* and an apparent evolution of its orientation. Our reconstruction is slightly more resolved, showing small scale structures on the ring, and comes with uncertainty quantification via samples. In addition to the emission ring, we find a significant and potentially fading emission structure south-west of it. All this demonstrates methodological readiness for further VLBI observations of strongly varying sources.

Methods

Our method is based on Bayesian statistics. The central quantity is the negative logarithmic posterior probability of our latent variables which parametrise the sky brightness distribution. This logarithmic probability density, called the information Hamiltonian, is composed of the logarithmic likelihood and the prior. The posterior mean and its uncertainty are obtained with MGVI, which requires only the likelihood and its derivatives as input. In the following we further describe the components of the likelihood and our algorithm.

Likelihood The likelihood of the measured visibilities given the sky brightness distribution s is computed independently for each time frame. The visibilities for all measured data points are assumed to follow the measurement equation in the flat sky approximation:

$$R(s)_{AB} = \int e^{-2\pi i(u_{AB}x + v_{AB}y)} s(x, y) dx dy \quad (1)$$

$$= e^{\rho_{AB}} e^{i\phi_{AB}}. \quad (2)$$

Here AB runs through all ordered pairs of antennas A and B for all non-flagged baselines. The visibilities are complex numbers and we express them in polar coordinates in terms of logarithmic amplitudes $\rho_{AB}(s)$ and phases $\phi_{AB}(s)$. To avoid antenna based systematic effects, we compute

closure quantities from these visibilities [15]. Closure phases are obtained by combining a triplet of complex phases of visibilities via:

$$\varphi_{ABC} = \phi_{AB} + \phi_{BC} + \phi_{CA}. \quad (3)$$

Closure amplitudes are formed by combining the logarithmic absolute value of four visibilities:

$$\varrho_{ABCD} = \rho_{AB} - \rho_{BC} + \rho_{CD} - \rho_{DA}. \quad (4)$$

These closure quantities are invariant under antenna based visibility transformations of the form

$$R(s)_{AB} \rightarrow c_A c_B^* R(s)_{AB} \quad (5)$$

for all antennas and multiplicative calibration errors c_A and c_B^* , where $*$ denotes the complex conjugate. Note that forming the closure phases is a linear operation on the complex phase, while forming the closure amplitudes is linear in the logarithmic absolute value. We can thus represent these operations using matrices:

$$\varrho = L\rho, \quad \varphi = M\phi. \quad (6)$$

The closure matrices L and M are sparse and contain in every row ± 1 for antennas associated with the closure, and zero elsewhere. They are constructed such that they correspond to a maximal non-redundant set of closure quantities. Closure sets are non-redundant if and only if

$$\text{rank}(L) = \dim(\varrho) \quad \text{and} \quad \text{rank}(M) = \dim(\varphi), \quad (7)$$

and they are maximal if no closure phase or amplitude can be added without violating these conditions. This means that out of the set of all possible closure quantities, only a limited number can be chosen before redundancies occur. We build the closure sets to be used in the imaging with help of a greedy algorithm taking those quantities with better signal-to-noise ratio first.

We compute the observed closure quantities ϱ_d and φ_d from the published visibility data $d = e^{\rho_d} e^{i\phi_d}$ as:

$$\varrho_d = L\rho_d \quad \text{and} \quad \varphi_d = M\phi_d. \quad (8)$$

In a first order approximation, which is valid for sufficiently high signal-to-noise ratio, the noise covariances N_ϱ and N_φ on the closure quantities are related to the visibility error RMS vector σ due to thermal noise via:

$$N_\varrho = LNL^\dagger \quad \text{and} \quad N_\varphi = MNM^\dagger, \quad \text{with } N = \text{diag} \left(\frac{\sigma^2}{|d|^2} \right), \quad (9)$$

with $\text{diag}(x)$ denoting a diagonal matrix with x on its diagonal. Here, we assume a Gaussian distribution of the visibility errors, while taking into account the non-diagonal noise contributions to the closure quantities introduced by applying the matrices L and M :

$$\mathcal{P}(\varrho_d | \varrho, L, N) = \mathcal{N}(\varrho_d | \varrho, N_\varrho), \quad (10)$$

$$\mathcal{P}(e^{i\varphi_d} | \varphi, M, N) = \mathcal{N}(e^{i\varphi_d} | e^{i\varphi}, N_\varphi). \quad (11)$$

$\mathcal{N}(\psi | \bar{\psi}, \Psi)$ denotes a Gaussian distribution over ψ with mean $\bar{\psi}$ and covariance Ψ . Note that we do not directly use the complex phases, but their position $e^{i\varphi_d}$ on the complex unit circle, which mitigates the problem of phase wraps at the price of approximating the corresponding covariance.

Modeling the sky brightness The sky brightness distribution $s_{xt\nu}$ is defined within a fixed field of view $\Omega_x \subset \mathbb{R}^2$, a time interval $\Omega_t = [0, \bar{t}]$, and frequency range $\Omega_\nu \subset \mathbb{R}$, which renders it to be a field defined in space, time, and frequency. We assume s to be a priori log-normal distributed:

$$s_{xt\nu} := e^{\tau_{xt\nu}} \text{ with } x \in \Omega_x, t \in \Omega_t, \text{ and } \nu \in \Omega_\nu \text{ with } \mathcal{P}(\tau|T) := \mathcal{N}(\tau|0, T). \quad (12)$$

The a priori correlation structure of the logarithmic sky brightness is encoded within the covariance T . Choosing a log-normal model allows the sky brightness to vary exponentially on linear spatial, temporal, or frequency scale and ensures the positivity of the reconstructed intensity. We perform a basis transformation to a standardised Gaussian distribution $\mathcal{P}(\xi_s) = \mathcal{N}(\xi_s|0, \mathbb{1})$, which allows us to separate the correlation structure from its realisation [16]. The new coordinates ξ_s have the same dimension as the original parameters, but are a priori independent:

$$s = e^{A\xi_s} \text{ with } AA^\dagger := T. \quad (13)$$

This defines a generative model which turns standard normal distributed DOFs ξ_s into random variables s that are distributed according to (12). Although the information encoded in a distribution is invariant under coordinate transformations, MGVI depends on the choice of coordinates. Therefore, reformulating the entire inference problem in terms of standardised generative models is important to ensure that the prior information is fully captured by an approximation via MGVI.

Correlations in space, time, and frequency We do not know the correlation structure of the logarithmic sky brightness a priori, so we include it as part of the model, which has to be learned from the data. The different dimensions of the sky brightness are governed by completely distinct physical phenomena, which should be reflected in the model. Setting up such correlations involves a number of intricate technicalities which have to be dealt with. The main idea is to model the correlations in space, time, and frequency independently using the same underlying model and later combine them via outer products. Doing this naively results in degenerate and highly un-intuitive model parameters. The model we will be introducing in the following avoids these issues, but unfortunately requires a certain complexity.

We will start with the discussion with correlations along the different directions individually. A priori we do not want to single out any specific location or direction for the logarithmic sky brightness, which corresponds to statistical homogeneity and isotropy. According to the Wiener-Khinchin theorem, such correlation structures $T^{(i)}$ with $i \in \{x, t, \nu\}$ are diagonal in the Fourier domain and can be expressed in terms of a power spectrum $p_{T^{(i)}}(|k|)$:

$$T_{kk'}^{(i)} = \left(FT^{(i)} F^\dagger \right)_{kk'} \propto \delta(k - k') p_{T^{(i)}}(|k|), \quad (14)$$

where F denotes the Fourier transformation into the eigenbasis of $T^{(i)}$. As we build the model in terms of standardised coordinates, we will be working with the square root of the correlation matrix:

$$A_{kk'}^{(i)} \propto \delta(k - k') \sqrt{p_{T^{(i)}}(|k|)} =: \delta(k - k') p^{(i)}(|k|). \quad (15)$$

The amplitude spectrum $p^{(i)}(|k|)$ depends on the characteristic length scales of the underlying physical processes, which we do not precisely know. Our next task is to develop a flexible model for this spectrum that expresses our uncertainty and is compatible with a wide range of possible systems. Mathematically, we have to demand positivity of the amplitudes, which we enforce by modeling a logarithmic amplitude spectrum:

$$p^{(i)}(|k|) \propto e^{\gamma^{(i)}(|k|)}. \quad (16)$$

We do not want to impose any functional basis for this logarithmic amplitude spectrum $\gamma^{(i)}(|k|)$, so we describe it non-parametrically using an integrated Wiener process in logarithmic $l = \log|k|$ coordinates. This corresponds to a smooth, i.e. differentiable function, with correlation and exponential scale dependence, properties many physical systems exhibit. In the logarithmic coordinates l , the zero-mode, i.e. $|k| = 0$ is infinitely far away from all other modes. We will later on deal with it separately and we continue for now with all remaining modes. The integrated Wiener process in logarithmic coordinates $\gamma^{(i)}(l)$ reads:

$$\gamma^{(i)}(l) = c_0 + m^{(i)}l + \eta^{(i)} \int_{l_0}^l \int_{l_0}^{l'} \xi_W^{(i)}(l'') dl' dl''. \quad (17)$$

Here c_0 is an integration constant we ignore for now, as its degree of freedom will later on be explicitly parameterised in terms of a more intuitive quantity. The parameter $m^{(i)}$ is the slope of the amplitude on double-logarithmic scale and describes the preferred power law. It is a highly influential quantity, as it controls the overall smoothness of the logarithmic sky brightness distribution. The parameter $\eta^{(i)}$ describes how strongly the amplitude spectrum deviates smoothly from the power law. The precise shape of these deviations is encoded in the realisation $\xi_W^{(i)} \sim \mathcal{N}(\xi_W^{(i)}|0, \mathbb{1})$, which are also parameters of our model and follow a priori the standard Gaussian distribution. We do not want to fix the slope and deviations as they should be learned from the data. We impose Gaussian and log-normal priors with preference for a certain value and expected deviations for the slope and the deviations respectively:

$$m^{(i)} = \mu_m^{(i)} + \sigma_m^{(i)} \xi_m^{(i)}, \quad \eta^{(i)} = e^{\mu_\eta^{(i)} + \sigma_\eta^{(i)} \xi_\eta^{(i)}} \quad \text{with} \quad \xi_j^{(i)} \sim \mathcal{N}(\xi_j^{(i)}|0, \mathbb{1}), \quad j \in \{m, \eta\}. \quad (18)$$

The amplitude spectrum defines how strongly the log-brightness varies around its mean. These fluctuations have a severe impact on a priori plausible brightness distributions. Unfortunately, the relation of the hyper-parameters of this integrated Wiener process model to the overall variance is highly un-intuitive, but it is critical to constrain them to reasonable values. Our strategy here is to divide out the degrees of freedom associated with the fluctuations and introduce a new parameter to constrain this quantity directly. The real-space variation $\tilde{U}^{(i)}$ of the logarithmic sky brightness with a correlation structure associated with the integrated Wiener process is given by the integration over all modes except the first:

$$\tilde{U}^{(i)} := \int_{k \neq 0} e^{2\gamma^{(i)}(|k|)} dk. \quad (19)$$

We replace this variation with a new parameter $a^{(i)}$ that describes the magnitude of expected fluctuations:

$$p^{(i)}(|k|) = a^{(i)} \frac{e^{\gamma^{(i)}(|k|)}}{\sqrt{\tilde{U}^{(i)}}}, \quad \forall k \neq 0. \quad (20)$$

This step allows us to remove the integration constants c_0 (which we ignored previously) from the Wiener processes and replace them with $a^{(i)}$. We also learn these parameters from the data directly and impose a log-normal model analogous to $\eta^{(i)}$ with hyper-parameters $\mu_a^{(i)}$ and $\sigma_a^{(i)}$.

We will now combine correlation structures in independent directions. For every sub-domain, in our case space, time, and frequency, we use an instance of the model described above. We have not yet specified how to deal with the amplitude of the zero-modes $p^{(i)}(0)$, and their treatment will emerge from the combination of the sub-directions. The overall correlation structures of all directions will be given by the outer product of the sub-spaces:

$$A = \bigotimes_{i \in \{x, t, \nu\}} A^{(i)}. \quad (21)$$

Building the model in this way is problematic, as this product has redundant multiplicative degrees of freedom with positive numbers, i.e. $\alpha(A^{(i)} \otimes A^{(j)}) = (\alpha A^{(i)}) \otimes A^{(j)} = A^{(i)} \otimes (\alpha A^{(j)})$. With every additional direction we add one additional degenerate degree of freedom. We can use this freedom to constrain the zero-mode of the amplitude spectrum, and thus remove the degeneracy up to a global factor. For this we use the normalised amplitudes:

$$\tilde{A}^{(i)} := \left(\frac{1}{V^{(i)}} \int_{\Omega^{(i)}} A_{i0}^{(i)} \right)^{-1} A^{(i)}. \quad (22)$$

With the appropriate Fourier convention,

$$p^{(i)}(0) = \int_{\Omega^{(i)}} A_{i0}^{(i)}, \quad (23)$$

we see that the zero-mode of the normalised amplitude $\tilde{A}^{(i)}$ is fixed to the total volume $V^{(i)}$ of the space $\Omega^{(i)}$. Consequently, the overall correlation structure can be expressed in terms of

$$A = \alpha \bigotimes_{i \in \{x, t, \nu\}} \tilde{A}^{(i)}. \quad (24)$$

The remaining multiplicative factor α globally sets the scale in all directions and has to be learned from the data. We will also put a log-normal prior with log-mean μ_α and log-variance σ_α hyper-parameters and corresponding standard Gaussian parameters ξ_α on this quantity.

This was the last ingredient for the correlation structure along multiple independent directions. We will briefly summarise all the required hyper-parameters and how the generative model for the correlation structure is built. We start with the correlations in the individual directions $A^{(i)}(\xi^{(i)})$. We describe them in terms of their amplitude spectrum. Four distinct standardised model parameters are learned from the data $\xi^{(i)} := (\xi_m^{(i)}, \xi_\eta^{(i)}, \xi_W^{(i)}, \xi_a^{(i)})$. The first describes the slope of the linear contribution to the integrated Wiener process. The second is related to the strength of the smooth deviations from this linear part. The third parameter describes the actual form of these deviations. Finally, the last one describes the real-space fluctuations of the associated field. The hyper-parameters are μ_j^i and σ_j^i for $j \in \{m, \eta, a\}$ specifying the expected mean and standard deviation of the slope $m^{(i)}$ and log-quantities for the other two. In addition to these, we have to determine the global scale parameter $\alpha(\xi_\alpha)$, where we also specify its logarithmic mean μ_α and standard deviation σ_α . The generative model for the correlation structure is therefore:

$$A(\xi_A) = \alpha(\xi_\alpha) \bigotimes_{i \in \{x, t, \nu\}} \tilde{A}^{(i)}(\xi^{(i)}). \quad (25)$$

Combining this with the generative model for the sky brightness itself we end up with the full model:

$$s(\xi) = e^{A(\xi_A)\xi_s}. \quad (26)$$

All parameters of our model are now standardised and follow a standard Gaussian distribution. The Bayesian inference problem is fully characterised by the negative logarithm (or information) of the joint probability distribution of data and parameters. Combining the closure likelihoods with the described sky brightness model therefore yields:

$$\begin{aligned} -\log \left(\mathcal{P}(\varrho_d, e^{i\varphi_d}, \xi) \right) &= \frac{1}{2} \left(\varrho_d - \varrho(s(\xi)) \right)^\dagger N_\varrho^{-1} \left(\varrho_d - \varrho(s(\xi)) \right) \\ &\quad + \frac{1}{2} \left(e^{i\varphi_d} - e^{i\varphi(s(\xi))} \right)^\dagger N_\varphi^{-1} \left(e^{i\varphi_d} - e^{i\varphi(s(\xi))} \right) \\ &\quad + \frac{1}{2} \xi^\dagger \xi + H_0, \end{aligned} \quad (27)$$

where H_0 is a constant that is independent of the latent variables ξ .

Metric Gaussian Variational Inference So far we developed a probabilistic model in the generative form of the joint distribution of data and model parameters. In the end we want to know what the data tells us about the model parameters, as given in the posterior distribution according to Bayes' theorem. Our model is non-conjugate and we cannot solve for the result analytically. Instead, we will approximate the true posterior distribution with a Gaussian using variational inference. We will use Metric Gaussian Variational Inference (MGVI), which allows us to capture posterior correlations between all model parameters despite the 7.4 million parameters. MGVI is an iterative scheme that performs a number of subsequent Gaussian approximations $\mathcal{N}(\xi|\bar{\xi}, \Xi)$ to the posterior distribution. Instead of learning a parametrised covariance, an expression based on the Fisher information metric evaluated at the intermediate mean approximations is used, i.e. $\Xi \approx I(\xi)^{-1}$, with

$$I(\xi) = \frac{\partial \varrho(s(\xi))}{\partial \xi} N_{\varrho}^{-1} \left(\frac{\partial \varrho(s(\xi))}{\partial \xi} \right)^{\dagger} + \frac{\partial e^{i\varphi(s(\xi))}}{\partial \xi} N_{\varphi}^{-1} \left(\frac{\partial e^{i\varphi(s(\xi))}}{\partial \xi} \right)^{\dagger} + \mathbb{1} . \quad (28)$$

The first two terms originate from the likelihood and the last from the prior. All these are expressed in terms of computer routines and we do not have to store this matrix explicitly. This is a non-diagonal matrix capturing correlations between all parameters. To learn the mean parameter $\bar{\xi}$ we minimise the Kullback-Leibler divergence between the true posterior and our approximation:

$$\mathcal{D}_{\text{KL}}(\mathcal{N}(\xi|\bar{\xi}, \Xi) || \mathcal{P}(\xi|\varphi_d, \varrho_d)) = \int d\xi \mathcal{N}(\xi|\bar{\xi}, \Xi) \ln \left(\frac{\mathcal{N}(\xi|\bar{\xi}, \Xi)}{\mathcal{P}(\xi|\varphi_d, \varrho_d)} \right) . \quad (29)$$

This quantity is an expectation value over the Gaussian approximation and measures the overlap between true posterior and our approximation. As we minimise this quantity, the normalisation of the posterior distribution is irrelevant and we can work with the joint distribution over data and model parameters, as given by (27). We estimate the KL-divergence stochastically by replacing the expectation value through a set of samples from the approximation. The structure of the implicit covariance approximation allows us to draw independent samples from the Gaussian for a given location.

$$\xi^* \sim \mathcal{N}(\xi|0, \Xi), \text{ therefore } \bar{\xi} \pm \xi^* \sim \mathcal{N}(\xi|\bar{\xi}, \Xi). \quad (30)$$

Using the mean of the Gaussian plus and minus samples corresponds to antithetic sampling, which reduces the sampling variance significantly, leading to performance increases. MGVI now iterates between drawing samples for a given mean parameter and optimising the mean given the set of samples. The main meta-parameters of this procedure are the number of samples and how accurately the intermediate approximations are performed. The procedure converges once the mean estimate $\bar{\xi}$ is self-consistent with the approximate covariance. To minimise the KL-divergence, we rely on efficient quasi-second-order Newton-Conjugate-Gradient in a natural gradient descent scheme. In the beginning of the procedure, the accuracy of KL and gradient estimates, as well as overall approximation fidelity, will not be as important. In practice we gradually increase the accuracy to gain overall speedups.

Implementation We implement the generative model in NIFTy [5], which also provides an implementation of MGVI utilising auto-differentiation. We represent the spatial direction with 256×256 pixels, each with a length of $1 \mu\text{as}$. In the time direction we choose a resolution of 6 hours for the

entire observation period of 7 days, thus obtaining 28 time frames. We add another 28 frames to avoid artifacts from the periodic boundary conditions of the Fast Fourier Transform.

For the frequency direction only two channels are available and we do not expect them to differ much from each other. Instead of learning the correlation along this direction, as we do for the spatial and temporal axis, we assume a correlation between the two channel on the 99% level a priori.

This adds another factor of 2 of required pixels to the reconstruction. For future reconstructions with deeper frequency sampling we can extend the model and treat this direction equivalently to the space and time directions. Overall we have to constrain $256 \times 256 \times 56 \times 2 + \text{power spectrum DOFs} \approx 7.4$ million pixel values with the data.

The Gaussian approximation to the closure likelihoods is only valid in high signal-to-noise regimes [15]. We increase the SNR-ratio by averaging the visibilities over the individual scans of ~ 2 minutes. We also remove the intra-site baselines of ALMA–APEX and SMT–JCMT and combine their visibilities to all other stations by noise-weighted averaging.

The hyper-parameter choices for the presented reconstruction are given in Table 2. This setting follows two main considerations. First, we want to be relatively agnostic in terms of the spatial direction. Constraining the a priori slope of the spatial amplitude to -1.5 ± 0.5 allows to express structures ranging from the rough Wiener process to the smooth integrated Wiener process within one standard deviation. Also the overall variance of the logarithmic sky brightness is only constrained within two e -folds around $e^{1.5}$. Second, we do not expect strong variability in the temporal direction due to the physical scale of the system, extending over several light-days. We express this through the slope of the temporal amplitude of -4 ± 0.5 , imposing long correlations in time, whereas the overall fluctuations are again relatively unconstrained. We strongly restrict deviations from power-law spectra in space and time. This is necessary due to the small amount of data.

The closure likelihoods are invariant under global translational symmetries which are not broken by the prior. Thus, the posterior distribution is multi-modal which leads to two problematic effects. First, the source can disappear in one place and re-appear somewhere else in the time-resolved setting. We aim to avoid this by demanding a strong correlation in the temporal direction. The second effect are multiple copies of the source throughout the field of view. We discourage this behavior by concentrating the flux in the center of the image with a weak Gaussian beam for the first 15 reconstruction steps. Similarly, the EHT collaboration enforced a centred image by starting with parameters corresponding to a Gaussian source in the centre of the image, as well as by restricting the overall field of view. In cases these issues do not appear, we obtain consistent results. For the here presented reconstruction we chose one of those.

The heuristic for MGVI is given in Table 3. We initialise our latent parameters to 1/10th of a prior sample. We start with a low number of antithetic samples and inaccurate steps and increase the accuracy throughout the procedure. For the initial 20 iterations, we only reconstruct the sky brightness and not the power spectra. After thirty iterations, the reconstruction does no longer change in a meaningful way and we regard it as converged. We base our scientific analysis on the final set of twenty samples plus their antithetic partners.

For the energy direction we only have two channels available for which we set an a priori difference of 1% as we do not expect them to differ much from each other.

Validation We validate our method on three synthetic examples. The first is a static disk with a constant brightness and blurred edges. In the second example we reconstruct a slowly rotating crescent, a toy-model of the vicinity around the black hole. The rotation allows us to demonstrate our sensitivity to the dynamics. In the final example we attempt to recover two Gaussian shapes

that approach and rotate around each other. This example allows us to illustrate how well we can distinguish individual sources.

For all examples we follow the M87* observation. Data is taken through simulated measurements of all baselines on the respective source and we add the reported thermal noise from the original observation. We have four eight-hour observations throughout the seven day period. The reconstruction follows the identical procedure as for M87*, only with a reduced spatial resolution of 128×128 pixels for computational reasons.

The results together with the ground truth are shown in Figure 4. As the likelihood is invariant under shifts, offsets in the reconstruction are to be expected. We are able to recover the shapes of the different examples, irrespective of the source being static or not.

The differences between reconstruction and signal are all within the uncertainty budget provided by MGVI.

The recovered spatial correlation structures for the log-brightness, as well as the brightness itself is shown in Figure 5. On logarithmic scales these agree well with the ground truth within the error bounds. Our examples do not have prominent small-scale features, so the ground truth drops off rapidly. We have only limited data on these scales due to the measurement setup, so the reconstruction is primarily informed by the prior distribution. There we favour power-law like behavior, which cannot fall as steeply as the chosen examples. On the large image scales, where we do have good data available, the correlation matches the ground truth exceptionally well, including characteristic features like the disk diameter.

We also perform an analysis on the parameters of the reconstructed crescent. The results for the recovered diameter d , width w and orientation angle η are shown in Table 4. Here we compare the ground truth to the analysis of the mean reconstruction, following the approach of the EHT collaboration, as well as the mean results of the analysis on the samples directly, which gives two different results, as well as ways to quantify the uncertainty. In both approaches we under-estimate the ring diameter. For the analysis on the mean image, the deviation is captured in the uncertainty, whereas the sample-based approach seems to report a too small uncertainty. This might also be due to a bias in the estimation of this quantity, as the samples, compared to the mean, contain small-scale structures. A similar behavior is also seen for the width of the ring, but the results are not too far off. Both approaches capture well the dynamic orientation angle.

References

1. Collaboration, T. E. H. T. *First M87 EHT Results: Calibrated Data* 2019.
2. Enßlin, T. A. Information theory for fields. *Annalen der Physik*, 1800127 (2018).
3. Bouman, K. L. *et al.* Reconstructing Video from Interferometric Measurements of Time-Varying Sources. *arXiv e-prints*, arXiv:1711.01357 (Nov. 2017).
4. Knollmüller, J. & Enßlin, T. A. Metric Gaussian Variational Inference. *arXiv preprint arXiv:1901.11033* (2019).
5. Arras, P. *et al.* NIFTy5: Numerical Information Field Theory v5. *Astrophysics Source Code Library* (2019).
6. Arras, P., Frank, P., Leike, R., Westermann, R. & Enßlin, T. A. Unified radio interferometric calibration and imaging with joint uncertainty quantification. *A&A* **627**, A134 (2019).
7. Rogers, A. *et al.* The structure of radio sources 3C 273B and 3C 84 deduced from the ‘closure’ phases and visibility amplitudes observed with three-element interferometers. *The Astrophysical Journal* **193**, 293–301 (1974).

8. Et al., T. E. C. First M87 Event Horizon Telescope Results. I. The Shadow of the Supermassive Black Hole. *ApJL* **875**, 1 (2019).
9. Et al., T. E. C. First M87 Event Horizon Telescope Results. II. Array and Instrumentation. *ApJL* **875**, 2 (2019).
10. Et al., T. E. C. First M87 Event Horizon Telescope Results. III. Data Processing and Calibration. *ApJL* **875**, 3 (2019).
11. Et al., T. E. C. First M87 Event Horizon Telescope Results. IV. Imaging the Central Supermassive Black Hole. *ApJL* **875**, 4 (2019).
12. Et al., T. E. C. First M87 Event Horizon Telescope Results. V. Physical Origin of the Asymmetric Ring. *ApJL* **875**, 5 (2019).
13. Et al., T. E. C. First M87 Event Horizon Telescope Results. VI. The Shadow and Mass of the Central Black Hole. *ApJL* **875**, 6 (2019).
14. Nalewajko, K., Sikora, M. & Róžańska, A. Orientation of the crescent image of M 87*. *A&A* **634**, A38 (Feb. 2020).
15. Blackburn, L. *et al.* Closure statistics in radio interferometric data. *arXiv preprint arXiv:1910.02062* (2019).
16. Kingma, D. P. & Welling, M. Auto-encoding variational Bayes. *arXiv preprint arXiv:1312.6114* (2013).
17. *Time-resolved reconstruction of M87** 2020. doi:10.5281/zenodo.3664583. <<https://doi.org/10.5281/zenodo.3664583>>.

Acknowledgements

We thank Landman Bester and Iniyan Natarajan for discussions regarding VLBI imaging, and the Schneefernerhaus for their hospitality. P.A. acknowledges the financial support by the German Federal Ministry of Education and Research (BMBF) under grant 05A17PB1 (Verbundprojekt D-MeerKAT).

Author Contributions

P.A., P.H., J.K and R.L. implemented and tested the likelihood and the overall inference algorithm. P.F. tested the likelihood and the overall inference algorithm. P.F. and P.A. contributed the amplitude model which features outer products of power spectra. M.R. provided implementations and numerical optimisation for many of the employed algorithms. T.E. coordinated the team, contributed to discussions and contributed text to this publication.

Data Availability

The data this work is based on has been published by the Event Horizon Collaboration [10, 11] and is available at [1]. We provide a set of 20 antithetic sample pairs of the sky brightness from the approximate posterior distribution, which can be used to propagate uncertainty to any derived quantity. The samples are available at [17].

List of Figures

- 1 Visualisation of the posterior mean. All figures are constrained to half the reconstructed field of view. The first row shows time frames of the image cube, one for each day. The second row visualises the absolute difference between adjacent days. Blue and red visualises increasing and decreasing flux over time, respectively. The third row visualises the relative difference in flux over time. The overplotted contour lines show the flux at 0.009, 0.023, 0.051, 0.188, 0.282, 0.376 Jy/ μas^2 of our posterior mean. 14
- 2 The first row shows the reconstructed mean and relative error, averaged over the entire observational period of 7 days. The first panel of the bottom row is a saturated plot of the time averaged posterior mean, revealing the emission zones outside the ring. The overplotted contour lines show flux at 0.009, 0.023, 0.051, 0.188, 0.282, 0.376 Jy/ μas^2 . The last panel on the bottom row shows the result of the EHT-imaging pipeline in comparison, also saturated and with overplotted contour lines. . 15
- 3 Time evolution of the flux for posterior samples and their ensemble mean at specific sky locations and areas as indicated in the central panel. The non-central panels show flux values of posterior samples (thin lines) and their mean (thick lines). Of those, the bottom right one displays the flux integrated inside (red) and outside the circle (green), as well as the sum of those (blue). For comparability all integrals are restricted to the field of view of the EHT collaboration image which is indicated by the black box in the central plot. The other non-central panels give local fluxes for the different locations labelled by numbers in the central panel. The corresponding fluxes of the single day EHT collaboration images are shown as points over a line for the observational time periods. 16
- 4 Results of our validation on synthetic observations. All fluxes are in units of mJy/ μas^2 . The ground truth signals are shown with their reconstructions directly beneath them. Time goes from left to right showing ground truth signals and their reconstructions at one day intervals. Different source models are shown from top to bottom: disk, crescent, double sources. The bottom bar chart visualises the number of closure quantities used for the reconstruction for each time bin. Each bar represents the amount of 227GHz (darker gray) and 229GHz (light gray) data points. The dashed lines indicate the connection of time frames with the shown images. 17
- 5 Spatial correlation power spectra of our reconstruction for the EHT-observation of M87* (top left panel) and our three validation data sets. The red curves show the empirical power spectrum of the flux density. The blue curves show the reconstructed power spectrum of the logarithmic flux density. For the three validation sets, the corresponding power spectra of the ground truth is plotted as a dashed line. 18
- 6 Comparison of our imaging result to that of the EHT-imaging pipeline. All panels have the same colorbar. The columns label the four days, for which observational data exists. The first row shows snapshot images from the EHT-imaging pipeline for each of the 4 days. The second row shows our mean reconstruction for the same time frame. The third and forth row each show one posterior sample from our imaging pipeline. 19

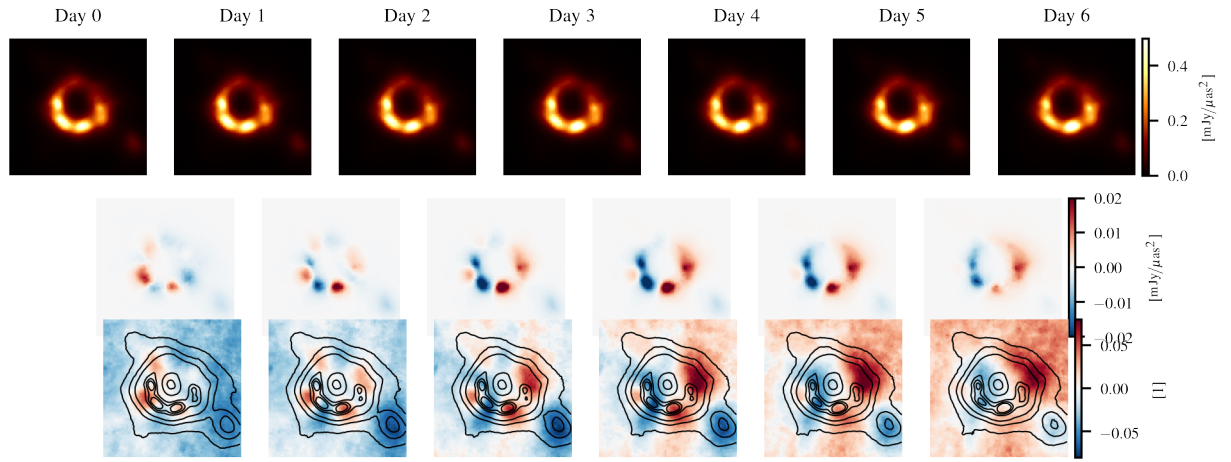


Figure 1: Visualisation of the posterior mean. All figures are constrained to half the reconstructed field of view. The first row shows time frames of the image cube, one for each day. The second row visualises the absolute difference between adjacent days. Blue and red visualises increasing and decreasing flux over time, respectively. The third row visualises the relative difference in flux over time. The overplotted contour lines show the flux at 0.009, 0.023, 0.051, 0.188, 0.282, 0.376 Jy/ μas^2 of our posterior mean.

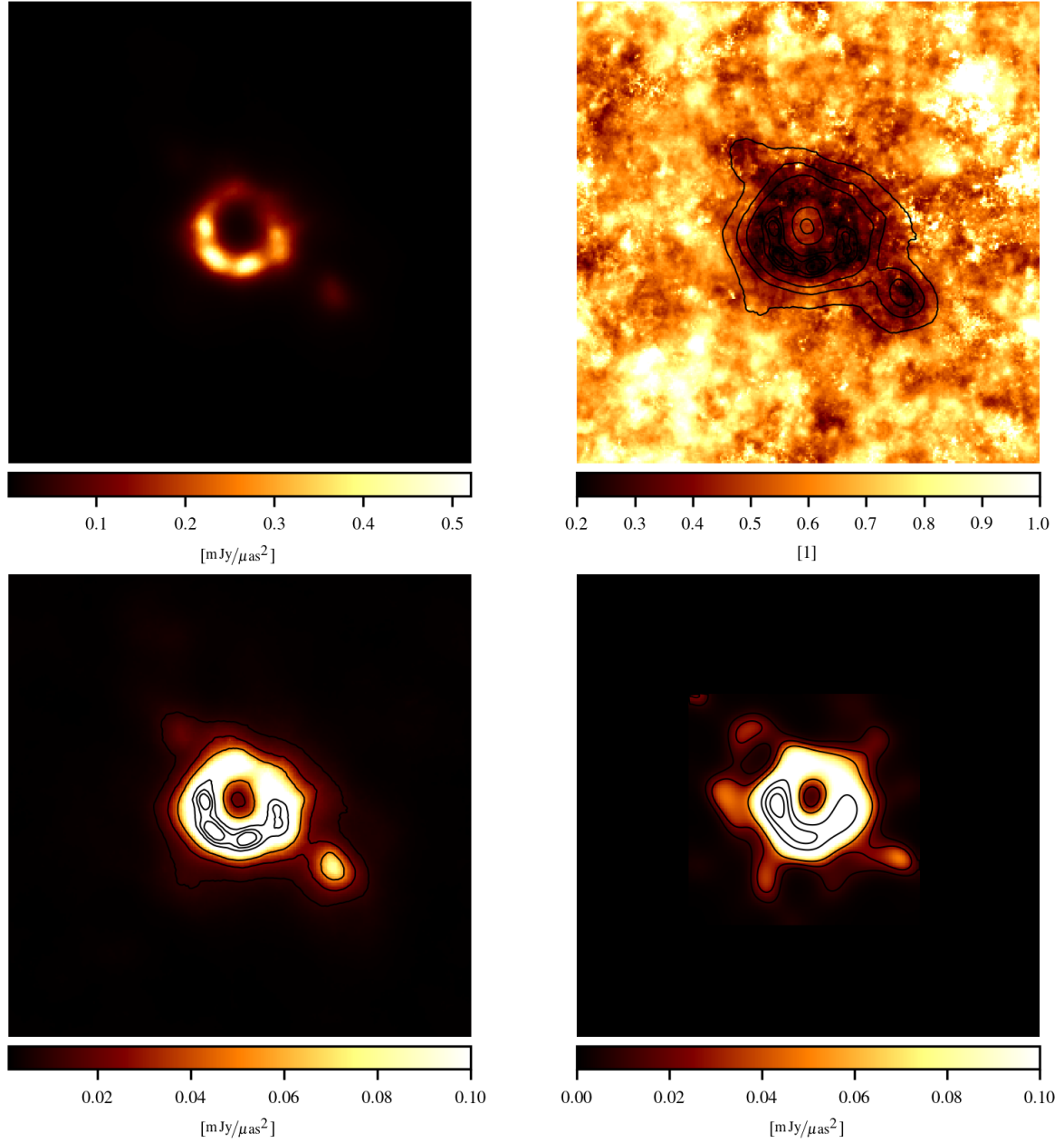


Figure 2: The first row shows the reconstructed mean and relative error, averaged over the entire observational period of 7 days. The first panel of the bottom row is a saturated plot of the time averaged posterior mean, revealing the emission zones outside the ring. The overplotted contour lines show flux at 0.009, 0.023, 0.051, 0.188, 0.282, 0.376 $\text{Jy}/\mu\text{as}^2$. The last panel on the bottom row shows the result of the EHT-imaging pipeline in comparison, also saturated and with overplotted contour lines.

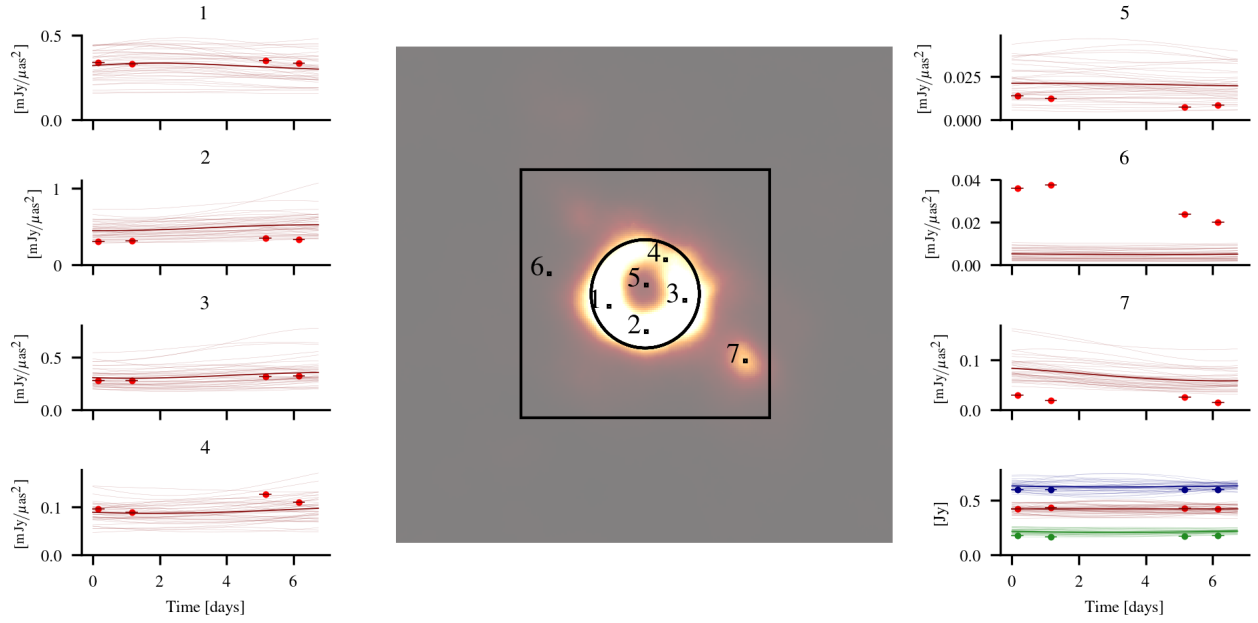


Figure 3: Time evolution of the flux for posterior samples and their ensemble mean at specific sky locations and areas as indicated in the central panel. The non-central panels show flux values of posterior samples (thin lines) and their mean (thick lines). Of those, the bottom right one displays the flux integrated inside (red) and outside the circle (green), as well as the sum of those (blue). For comparability all integrals are restricted to the field of view of the EHT collaboration image which is indicated by the black box in the central plot. The other non-central panels give local fluxes for the different locations labelled by numbers in the central panel. The corresponding fluxes of the single day EHT collaboration images are shown as points over a line for the observational time periods.

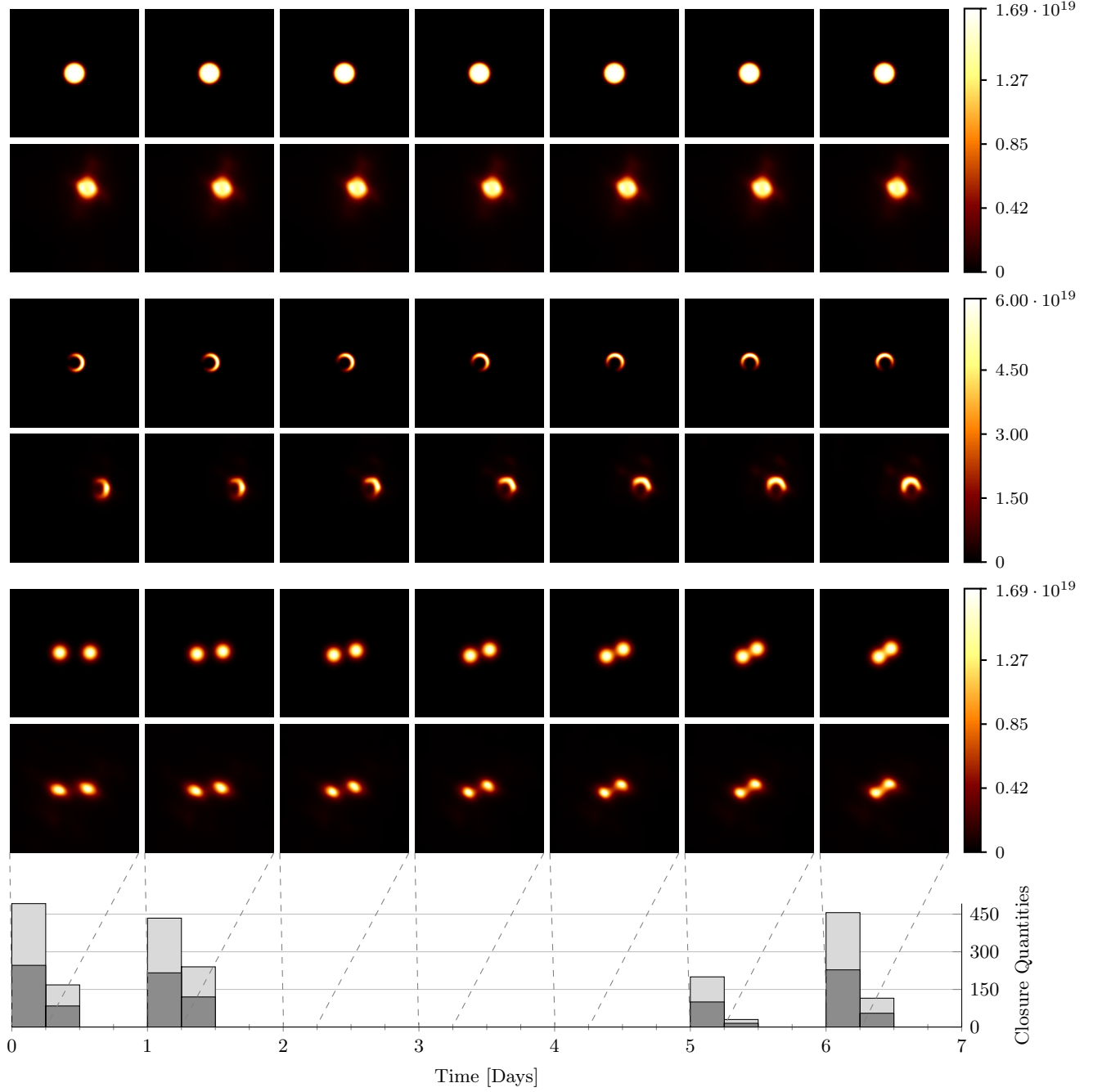


Figure 4: Results of our validation on synthetic observations. All fluxes are in units of $\text{mJy}/\mu\text{as}^2$. The ground truth signals are shown with their reconstructions directly beneath them. Time goes from left to right showing ground truth signals and their reconstructions at one day intervals. Different source models are shown from top to bottom: disk, crescent, double sources. The bottom bar chart visualises the number of closure quantities used for the reconstruction for each time bin. Each bar represents the amount of 227GHz (darker gray) and 229GHz (lighter gray) data points. The dashed lines indicate the connection of time frames with the shown images.

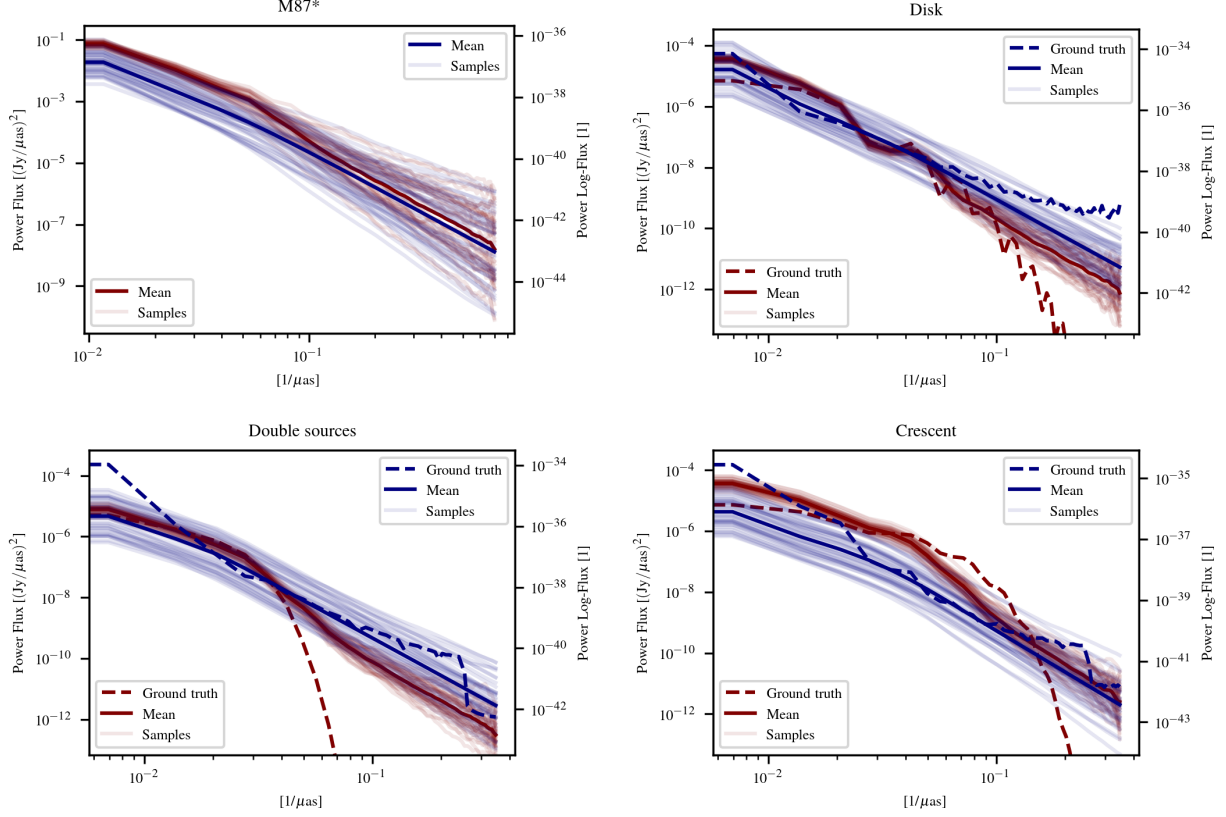


Figure 5: Spatial correlation power spectra of our reconstruction for the EHT-observation of M87* (top left panel) and our three validation data sets. The red curves show the empirical power spectrum of the flux density. The blue curves show the reconstructed power spectrum of the logarithmic flux density. For the three validation sets, the corresponding power spectra of the ground truth is plotted as a dashed line.

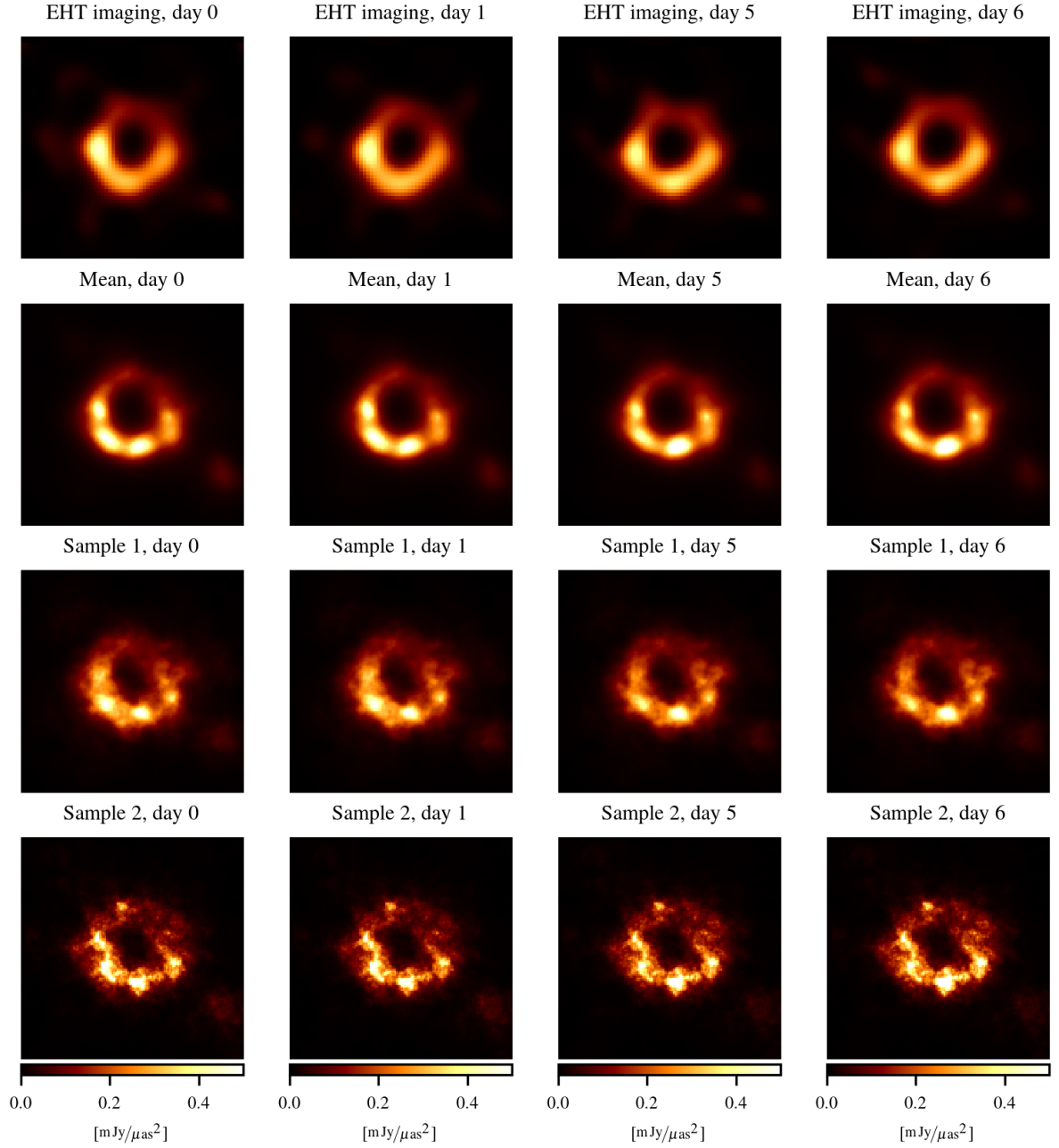


Figure 6: Comparison of our imaging result to that of the EHT-imaging pipeline. All panels have the same colorbar. The columns label the four days, for which observational data exists. The first row shows snapshot images from the EHT-imaging pipeline for each of the 4 days. The second row shows our mean reconstruction for the same time frame. The third and forth row each show one posterior sample from our imaging pipeline.

List of Tables

1	Comparison of diameter d , width w , orientation angle η , asymmetry A and floor-to-ring contrast ratio f_C as defined by [11, Table 7] and computed for images published by the EHT community (first three sections of table) as well as for our reconstruction (last two sections). Section four provides the result of the estimators and their uncertainties as defined by [11] applied to our posterior mean. Section five provides means and uncertainties based on processing our posterior samples individually through the estimators and by computing mean and standard deviations from these results. . .	21
2	The used hyper-parameters of the generative model.	22
3	Minimisation scheme used for the inference. In addition to the mentioned samples, their antithetic counterparts were used as well.	23
4	The crescent parameters recovered from the validation example, together with their underlying truth.	24

	$d (\mu\text{as})$	$w (\mu\text{as})$	$\eta (^\circ)$	A	f_C
DIFMAP					
April 5	37.2 ± 2.4	28.2 ± 2.9	163.8 ± 6.5	0.21 ± 0.03	5×10^{-1}
April 6	40.1 ± 7.4	28.6 ± 3.0	162.1 ± 9.7	0.24 ± 0.08	4×10^{-1}
April 10	40.2 ± 1.7	27.5 ± 3.1	175.8 ± 9.8	0.20 ± 0.04	4×10^{-1}
April 11	40.7 ± 2.6	29.0 ± 3.0	173.3 ± 4.8	0.23 ± 0.04	5×10^{-1}
EHT-IMAGING					
April 5	39.3 ± 1.6	16.2 ± 2.0	148.3 ± 4.8	0.25 ± 0.02	8×10^{-1}
April 6	39.6 ± 1.8	16.2 ± 1.7	151.1 ± 8.6	0.25 ± 0.02	6×10^{-2}
April 10	40.7 ± 1.6	15.7 ± 2.0	171.2 ± 6.9	0.23 ± 0.03	4×10^{-2}
April 11	41.0 ± 1.4	15.5 ± 1.8	168.0 ± 6.9	0.20 ± 0.02	4×10^{-2}
SMILI					
April 5	40.5 ± 1.9	16.1 ± 2.1	154.2 ± 7.1	0.27 ± 0.03	7×10^{-5}
April 6	40.9 ± 2.4	16.1 ± 2.1	151.7 ± 8.2	0.25 ± 0.02	2×10^{-4}
April 10	42.0 ± 1.8	15.7 ± 2.4	170.6 ± 5.5	0.21 ± 0.03	4×10^{-6}
April 11	42.3 ± 1.6	15.6 ± 2.2	167.6 ± 2.8	0.22 ± 0.03	6×10^{-6}
OUR METHOD (MEAN ANALYSIS LIKE [11, TABLE 7])					
April 5	40.7 ± 2.9	14.7 ± 3.9	161.0 ± 7.5	0.28 ± 0.04	1×10^{-4}
April 6	40.6 ± 2.8	14.6 ± 3.9	159.5 ± 7.4	0.28 ± 0.04	1×10^{-4}
April 10	41.1 ± 2.5	14.6 ± 3.8	174.7 ± 7.5	0.27 ± 0.03	1×10^{-4}
April 11	41.3 ± 2.5	14.6 ± 3.8	178.7 ± 8.0	0.26 ± 0.03	1×10^{-4}
OUR METHOD (SAMPLES)					
April 5	40.2 ± 1.1	13.4 ± 2.4	158.3 ± 4.5	0.28 ± 0.02	1×10^{-4}
April 6	40.3 ± 1.1	13.3 ± 2.5	157.1 ± 4.1	0.29 ± 0.02	1×10^{-4}
April 10	40.8 ± 1.2	13.3 ± 2.4	172.8 ± 4.4	0.27 ± 0.03	1×10^{-4}
April 11	41.0 ± 1.1	13.3 ± 2.5	176.6 ± 4.7	0.27 ± 0.03	1×10^{-4}

Table 1: Comparison of diameter d , width w , orientation angle η , asymmetry A and floor-to-ring contrast ratio f_C as defined by [11, Table 7] and computed for images published by the EHT community (first three sections of table) as well as for our reconstruction (last two sections). Section four provides the result of the estimators and their uncertainties as defined by [11] applied to our posterior mean. Section five provides means and uncertainties based on processing our posterior samples individually through the estimators and by computing mean and standard deviations from these results.

Parameter	Value
μ_α	0.2
σ_α	0.1
$\mu_a^{(x)}$	1.5
$\sigma_a^{(x)}$	1
$\mu_m^{(x)}$	-1.5
$\sigma_m^{(x)}$	0.5
$\mu_\eta^{(x)}$	0.01
$\sigma_\eta^{(x)}$	0.001
$\mu_a^{(t)}$	0.2
$\sigma_a^{(t)}$	1
$\mu_m^{(t)}$	-4
$\sigma_m^{(t)}$	0.5
$\mu_\eta^{(t)}$	0.01
$\sigma_\eta^{(t)}$	0.001

Table 2: The used hyper-parameters of the generative model.

MGVI Iterations	Samples	Natural Gradient Steps	Artificial beam	Constant spectra
1–10	1	15	✓	✓
11–15	2	15	✓	✓
16–20	2	15		✓
21–25	3	15		
26–28	10	20		
29–30	20	30		

Table 3: Minimisation scheme used for the inference. In addition to the mentioned samples, their antithetic counterparts were used as well.

	$d (\mu\text{as})$	$w (\mu\text{as})$	$\eta (^\circ)$
GROUND TRUTH			
April 5	30.0	12.0	-90.0
April 6	30.0	12.0	-72.9
April 10	30.0	12.0	-4.3
April 11	30.0	12.0	12.9
OUR METHOD (MEAN ANALYSIS LIKE [11, TABLE 7])			
April 5	23.6 ± 10.5	18.3 ± 7.6	-84.6 ± 5.5
April 6	25.7 ± 9.0	16.3 ± 7.0	-71.3 ± 1.6
April 10	28.5 ± 2.5	14.9 ± 4.2	-7.5 ± 2.2
April 11	28.4 ± 2.4	15.4 ± 4.7	12.3 ± 1.5
OUR METHOD (SAMPLES)			
April 5	25.3 ± 1.1	15.8 ± 1.6	-85.4 ± 4.7
April 6	26.7 ± 1.0	15.3 ± 1.5	-70.0 ± 3.6
April 10	28.3 ± 1.1	15.4 ± 1.5	-5.4 ± 3.8
April 11	28.1 ± 1.1	16.0 ± 1.7	14.2 ± 3.5

Table 4: The crescent parameters recovered from the validation example, together with their underlying truth.